CLAS-NOTE 95-014

Report to CEBAF on CLAS Region II Drift Chamber Prototype Work

Brian A. Raue, Charles Hyde-Wright, Andi Klein, Stephan Kloc
Sebastian E. Kuhn, Pat Lahiff, Andre Stevenson and Lawrence Weinstein
Old Dominion University
Norfolk, VA

Submitted to CEBAF
in fulfillment of the requirements
of CEBAF contract
CEBAF-93-P6644

July 1994

Abstract

This report details the material testing and preliminary prototyping work done for the CLAS region II drift chambers in order to decide the suitability of Stesalit 4411W as endplate material. The report describes the mechanical tests done to determine the strength and dimensional stability of the endplate material. It also describes the electrical properties of Stesalit 4411W. The report describes in detail the performance of a single-cell drift chamber made with Stesalit endplates. We found Stesalit 4411W to be an excellent material for the drift chamber endplates.

PART I

Introduction

The CLAS region II drift chambers will operate in the high magnetic-field region between the super-conducting coils of CLAS. It is obviously desirable to avoid any large motions ($\gtrsim$200 μ) of the wire-chamber endplates which may lead to damage to the wires. Such motions may arise in the case of a power failure and subsequent magnet quench if conducting endplates were used. For this reason we studied the feasibility of using a non-conducting material for the construction of the endplates. The material studied in the tests described below was Stesalit 4411W, a composite fiberglass and epoxy resin material.

A number of mechanical, electrical, and chamber performance issues needed to be addressed before 4411W was approved as the endplate material. The mechanical issues which were studied for this report include material strength and dimensional stability and/or accuracy of the machined material. Part II discusses the various mechanical tests and their results. Part III discusses tests of the surface resistivity of Stesalit 4411W. This included tests of 4411W coated with various resins and un-coated.

Most importantly, we studied the behaviour of a single-cell prototype chamber constructed with 4411W endplates. This included characterization of the chamber's dark current, gain, and efficiency, and medium-term stability (over several weeks). We have characterized the gain and efficiency as a function of position in the chamber. In particular, we have looked at these characteristics near the endplates and compared to the midplane behaviour. These tests are discussed in part IV.

PART II

Mechanical Aspects of Stesalit 4411W

According to the specifications given by Stesalit [1], 4411W has a number of attractive mechanical features. These include a relatively high tensile strength (250 N/mm^2) and modulus of elasticity (24000 N/mm^2) compared to other non-conducting materials that one could conceivably use for endplate material. The specification sheet also claims that 4411W can be precision machined with a high degree of accuracy.

2.1 Load Testing of Perimeter Attachment Holes

The final design of the endplates [2] includes several points of attachment which lie near the perimeter of the 2 cm thick endplate. Because some of these attachment points consist of relatively large diameter holes (compared to the endplate thickness) and potentially bear substantial loads (up to a few hundred pounds), one must be concerned with the endplate material breaking or being inelastically deformed when under load. The attachment configuration which we tested is shown in figure 2.1. This is similar to the hole configuration in the final endplate design for the spring and block mounts.

The goal here was to test the strength of the 4411W under loading conditions similar to what is expected when the chambers are being constructed and installed. To do this a spring fixture was mounted in the hole shown in fig. 2.1. A 200 cm long steel pipe was attached to the spring while the endplate material was mounted rigidly in a vertical orientation (fig. 2.2). The pipe weighed 2.3 kg (5 lbs). This caused a deflection of both the endplate material and the pipe so that point W, 100 cm from the endplate, was displaced 3.5 cm from the horizontal. A 45.5 kg

(100 lbs) weight was hung from point W causing a 20 cm vertical displacement of W.

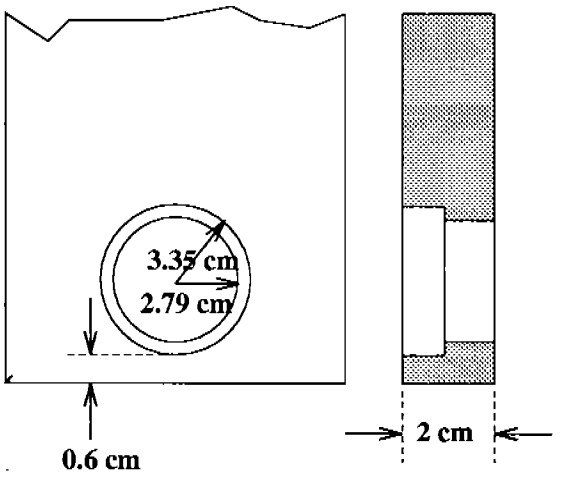

Figure 2.1: Top and side view sketches of a typical mounting hole in the endplate material.

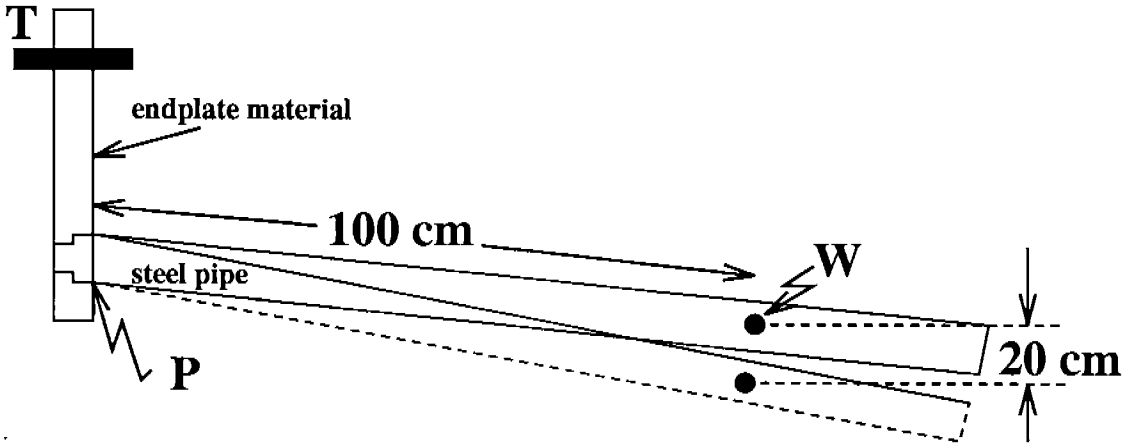

Figure 2.2: Side view sketch showing configuration for perimeter loading tests. Endplate material was rigidly mounted to a heavy table at point T. Weight was hung from the steel pipe from point W. The dashed lines show the displacement of the pipe after hanging the weight.

When the weight was removed the pipe returned to the pre-loaded position indicating that no permanent distortion of endplate material occurred. There was also no visible damage, such as fractures or delamination, to the endplate material. The torque about point **P** of 450 N·m resulting from the above test is equivalent to hanging 2320 kg (5100 lbs) two centimeters from point **P**. Two centimeters is a similar distance scale to what we expect in the process of fabrication and installation of the wire chambers. However, we expect the weights involved to be a factor of ten less. Therefore we conclude that it is highly unlikely the endplates will be damaged during any of the fabrication or installation processes.

2.2 Test of Finite Element Analysis Modeling of Stesalit 4411W

Throughout the design of the endplates and various mechanical supports we have relied heavily on the results of finite element analysis (FEA) calculations [3]. It is obviously important that these calculations agree reasonably well with the real world situations. To check the reliability of the calculations we have measured deflections of the endplate material under various loads in a simple geometric configuration (fig. 2.3). In the test a 50x50 cm^2 piece of 2 cm thick 4411W was oriented in a horizontal plane and supported at the four corners (1cm from each edge) by 0.5 cm diameter pins. A 5 cm diameter aluminum foot was placed in the center of the plate on which a mass of 22.7 kg (10 lbs) was placed. A dial indicator with a 0.5 cm diameter hemispherical foot was used to determine the relative height of the endplate material at several points on the surface of the plate. The raw vertical deflections (δ_{meas}) of the plate are given in table 2.1a. The systematic uncertainty in the measurements is $\pm 6\mu$m which is a combination of the measurements' reproducibility and the precision to which the dial indicator can be read.

A portion of the vertical displacement is the result of compression or displacement of the corner support. This must be taken into account for comparison to the calculations. The displacement of the corners 1, 2, 3, and 4 (as labeled on fig. 2.3 were 6, 24, 6, and 18 μm respectively under the 22.7 kg load. The support points obviously did not displace uniformly. We have assumed that the corners

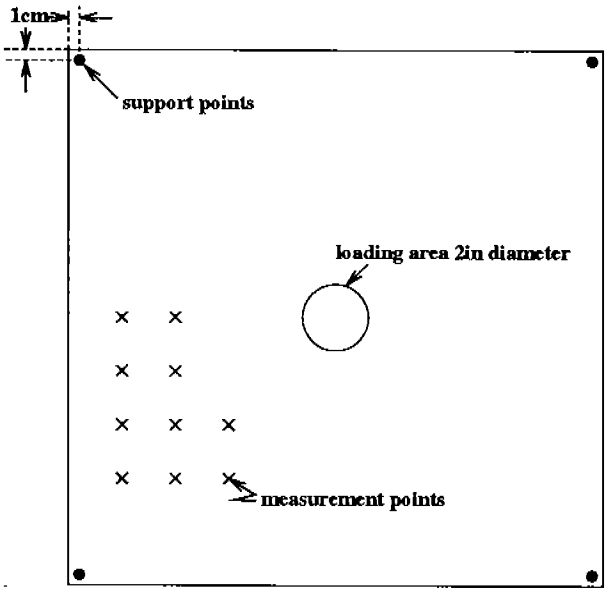

Figure 2.3: Top view sketch of setup for test of finite element analysis calculations.

1,2, and 4 define a plane which then allows us to calculate the displacement (δ_{sup}) at the points given in table 2.1a due to the displacement of the support points. The corrected deflections ($\delta_{meas} - \delta_{sup}$) of the endplate material are given in 2.1b.

The results of the FEA calculation (δ_{calc}) are given in table 2.1c and the difference between the measured and calculated deflections ($(\delta_{meas} - \delta_{sup}) - \delta_{calc}$) are given in table 2.1d. There is a 5 μm uncertainty in the calculated values. We see that the calculation agrees well with the measurements at all but one point (x=10, y=25). This simple test suggests that the FEA calculations are reliable. In fact, it is far better than the 10 to 20% difference between calculations and measured deflections typically found in many applications of FEA.

2.3 Accuracy of Standard Machining Techniques for Stesalit

Because of the high degree of accuracy involved in the construction of the region II drift chambers it is necessary that the endplate material can be manufactured to small tolerances using standard machining techniques. It is conceivable that

Table 2.1: **a:** Raw displacement (δ_{meas}) of endplate material. **b:** Deflection corrected for displacement of corner supports ($\delta_{meas} - \delta sup$). **c:** Deflection calculated by FEA (δ_{calc}). **d:** Difference between measured and calculated deflections ($(\delta_{meas} - \delta_{sup}) - \delta_{calc}$). Coordinates are given in cm from the edge of the endplate material and displacements/deflections are given in μm.

a	δ_{meas}			b	$\delta_{meas} - \delta_{sup}$		
	x (cm)				x (cm)		
y (cm)	5	10	15	y (cm)	5	10	15
10	67	83	108	10	57	71	95
15	99	105	114	15	87	91	99
20	111	121	-	20	97	106	-
25	111	140	-	25	95	123	-
c	δ_{calc}			d	$(\delta_{meas} - \delta_{sup}) - \delta_{calc}$		
	x (cm)				x (cm)		
y (cm)	5	10	15	y (cm)	5	10	15
10	58	77	90	10	-1	-6	5
15	77	90	105	15	10	1	-6
20	86	100	115	20	11	-4	-
25	90	105	-	25	5	18	-

non-uniformities or defects in the raw endplate material could lead to problems maintaining accuracy in some of the machining processes. Such problems include drill walk (lateral movement of the drill bit at the point of entry) and drill wander (lateral movement of the drill bit as it traverses the material) which are of particular concern for the small diameter (3.5 mm) holes for the wire trumpets. Of related concern is the accuracy of the wire hole diameter and diametric uniformity both of which must be maintained so the height of the trumpet above the endplate surface is uniformly within tolerances.

2.3.1 Drilled Hole Position and Diameter Accuracy

As a measurement of the accuracy to which wire holes can be drilled we had a grid of 15 × 25 holes cut into two pieces of 2 cm thick Stesalit 4411W and two pieces of off-the-shelf 2 cm thick G10. In one piece of each material the holes were cut using a 9/64" (3.57 mm) drill bit while in the other two pieces the holes were made by first drilling with a smaller bit followed by cutting with a 9/64" end mill. A precision computer-controlled machine was used to drill the holes in specified locations.

The finished pieces were then placed on a coordinate measuring machine to determine the position and diameter of randomly chosen holes relative to their specified locations and diameters. For all of the pieces the positions were within 42 μm of the specified locations. For all of the pieces, the hole diameter was within 100 μm of the specified diameter. The drilled Stesalit 4411W had the best precision with all hole positions within 26 μm and all hole diameters within the 25μm tolerance.

2.3.2 Trumpet Height Accuracy

Ultimately the wire hole diameter tolerance and uniformity will effect the height with respect to the surface of the endplate of a wire trumpet inserted in the hole. This, in turn, determines the position of the wire with respect to the hole. What is of most importance, and what could most easily be measured, is the height of a trumpet with respect to a plane defined by the average heights of all of the trumpets. This was done for trumpets placed in the 375 holes drilled into 4411W described above.

Figure 2.4 is a schematic of the the test apparatus. Ball bearings of $\frac{1}{8}$" diameter (uniform to better than can be measured with dial calipers or approximately 0.0002") were placed in each trumpet. A dial indicator was mounted on a stand so that the arm of the indicator moved normal to the plane of the endplate. The foot of the indicator was placed on each ball and the indicator reading was recorded. The relative trumpet heights were then fit to a plane. The difference between the fit and measured relative heights should then give the deviation of the trumpet height from the nominal position.

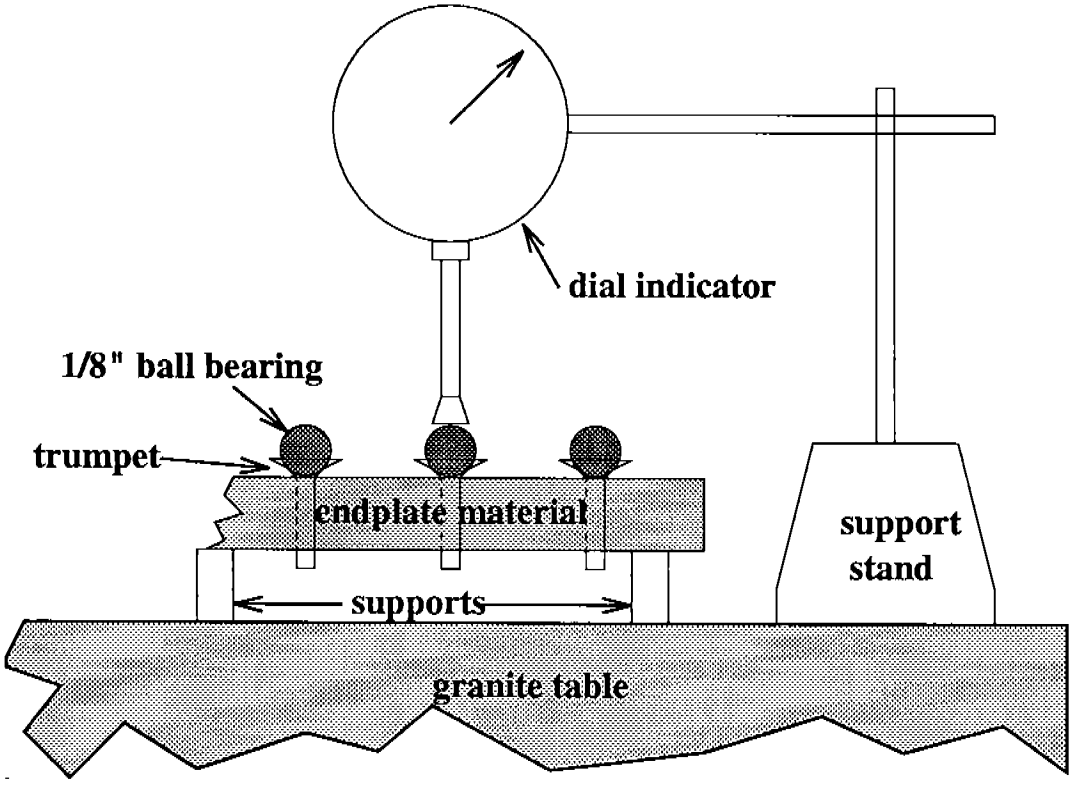

Figure 2.4: Schematic of trumpet-height test setup.

The results of these measurements are shown in fig. 2.5. Nearly all trumpets heights fall within $\pm 50\mu$m which satisfies wire positioning tolerances. The test clearly demonstrates that the drilling of holes in Stesalit 4411W is reproducible to small tolerances and also that this method of trumpet positioning is adequate to the task.

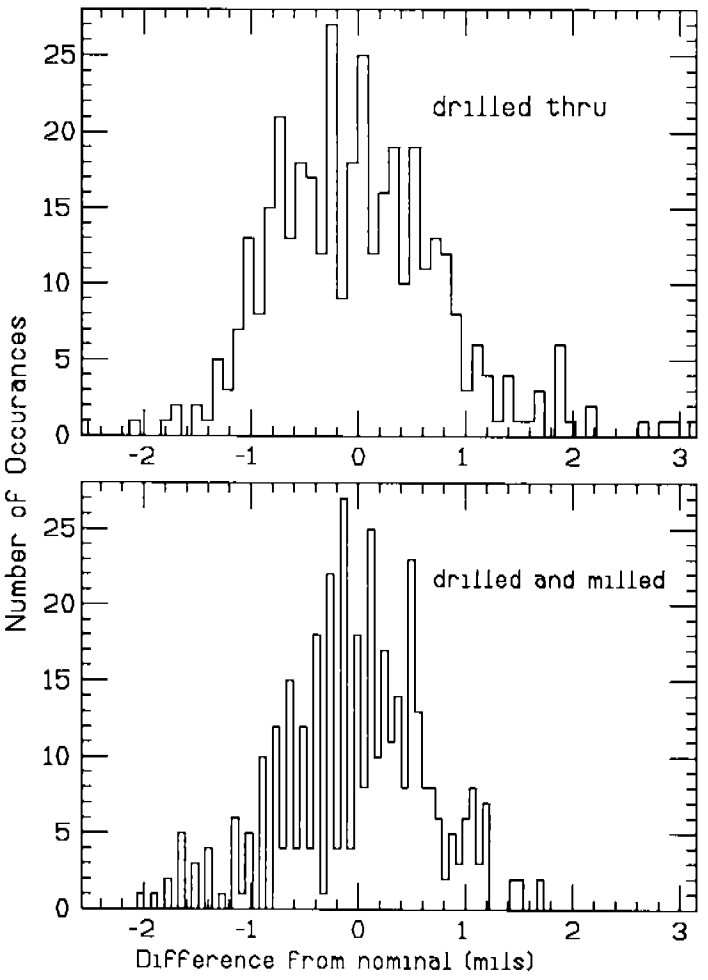

Figure 2.5: Trumpet-height deviation for two methods of hole drilling in Stesalit 4411W.

PART III

Surface Resistivity of Stesalit 4411W

One of the key considerations in choosing an endplate material is the surface resistivity. This must be appropriately chosen so that the dark current (current due to finite surface conductivity between sense and field wires) is minimized but any accumulated surface charge (due to ionizing processes in the chamber) is dissipated on the smallest possible time scale. A surface resistivity (ρ_{surf}) of 10^{13} to 10^{14} Ω/square is suitable with the lower end being preferable. With this in mind we have measured the surface resistivity of three types of coating: Stesalit's factory coating, 3M DP-190 epoxy, and un-coated Stesalit 4411W.

In the test setup (fig. 3.1) two copper-tape electrodes were placed on the endplate material's surface. The electrodes were uniformly separated by a distance s over a length l. One electrode was connected to the high-voltage output of a Bertan current-limiting power supply and the other was connected to ground. The voltage was then increased while the current draw was monitored through the supply's current monitor output using a high-precision electrometer. This was done over a voltage range starting at the lowest measurable current (1 nA) up to the point where a breakdown between electrodes occurred. The resulting current-versus-voltage data (fig. 3.2) were then fit with a straight line to give the average resistance, R. Table 3.1 summarizes the measurements and the results.

All three types of coating give surface resistivities in the desirable range. Of course the results of any such measurement will depend on the atmospheric conditions. In this case, most of the atmospheric conditions at test time could not be measured with any degree of accuracy. The ambient room temperature was about 22°C. We estimate the relative humidity to be 30-50%. As a point of comparison, the Stesalit specifications [1] give a surface resistivity of 1 to 3×10^{13} Ω/square for

4411W at 23°C and 50% relative humidity. It is not clear from the specifications if this refers to the coated or un-coated material. In either case, it is reasonable to assume that differences in atmospheric conditions, not to mention differences in measurement procedures, could easily account for the difference between measured and specified resistivity.

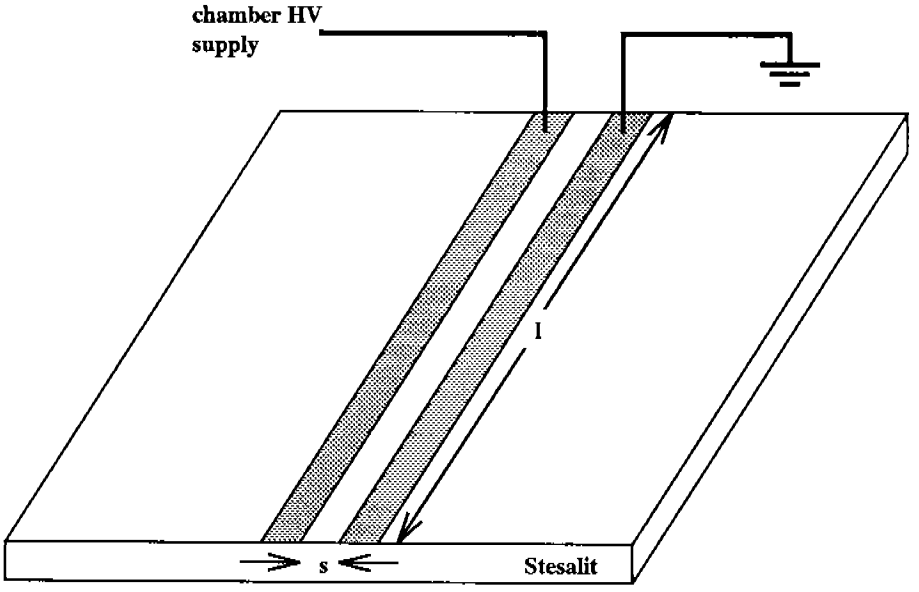

Figure 3.1: Test setup for measuring surface resistivity.

Table 3.1: Summary of resistivity measurements.

coating	s (mm)	l (mm)	R ($T\Omega$)	ρ_{surf} (Ω/sqare)
factory	2.7 ± 0.2	144 ± 1	1.4 ± 0.1	$7.5 \times 10^{13} \pm 0.8 \times 10^{13}$
3M DP-190	1.2 ± 0.2	75 ± 1	0.77 ± 0.06	$4.8 \times 10^{13} \pm 0.9 \times 10^{13}$
un-coated	1.6 ± 0.2	254 ± 1	0.48 ± 0.05	$7.6 \times 10^{13} \pm 1.2 \times 10^{13}$

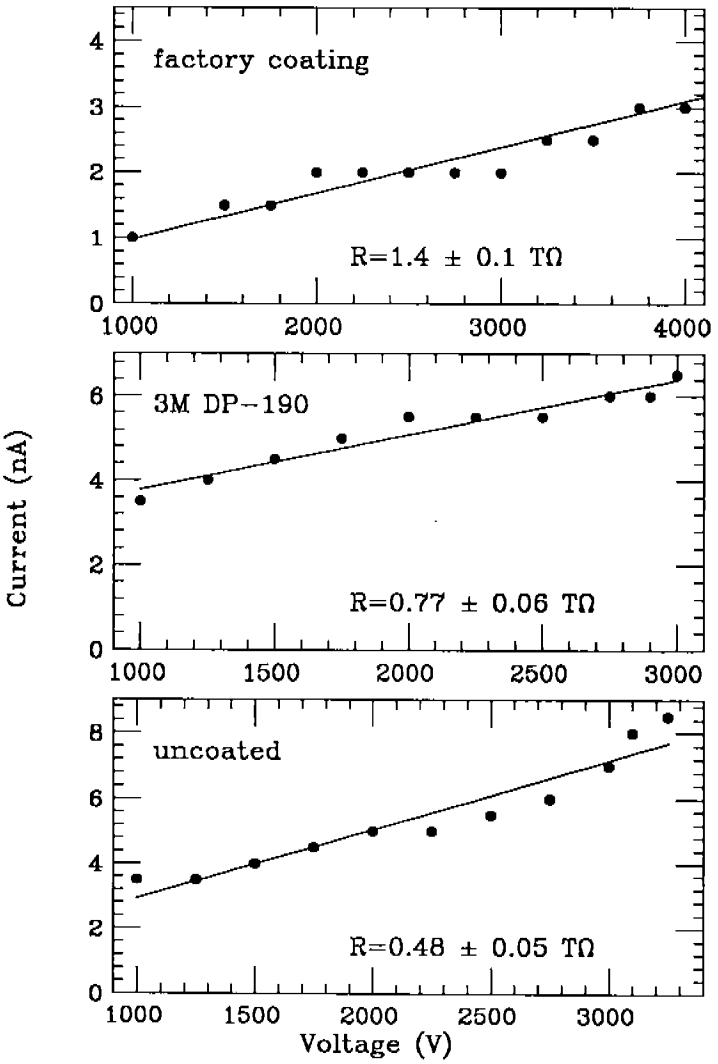

Figure 3.2: Current drawn vs applied voltage for coated materials as labeled.

PART IV

Single Cell Prototype (paramecium)

4.1 Basic Construction and Electronics

As a preliminary test of how the use of Stesalit 4411W affects the performance of a hexagonal-cell drift chamber, we constructed a single-cell prototype which is schematically shown in figure 4.1. The chamber has a single sense wire surrounded by six field-shaping wires arranged in the standard hexagonal-cell wire layout [4] of the CLAS drift chamber. Six guard wires lie outside the field wires and are biased so that the total charge approximately balances the charge on the field and sense wires. The chamber is surrounded on three sides with a grounded aluminized-nylon foil which acts as a gas barrier.

In order to match "final" operating conditions as closely as possible we utilized wire, connecting hardware, and tensions as similar to final design specifications as possible. We used region III trumpets, crimp pins and wire. The most noteworthy design difference from regions I and III is the trumpet positioning technique as discussed in section 2.3.2. The crimp pin was held in the trumpet by means of a solder connection. Wire tension was established by hanging weights from wire that had been connected at one end and then fed through the trumpet and crimp at the other end so that wire came through the trumpet in a vertical orientation. Weights of 150 g were used on the 150 μm gold-plated aluminum field and guard wires and 20 g on the 20 μm gold-plated tungsten sense wire.

Figure 4.2 is a schematic of the on-board electronics used for a majority of the tests of the single-cell prototype. Again, we attempted to match "final" designs as closely as possible. The field/guard wires were ganged to a common high voltage (HV) input so that all of the field/guard wires would be held at a common voltage. The HV for all wires was supplied by Bertan current-limiting supplies through a

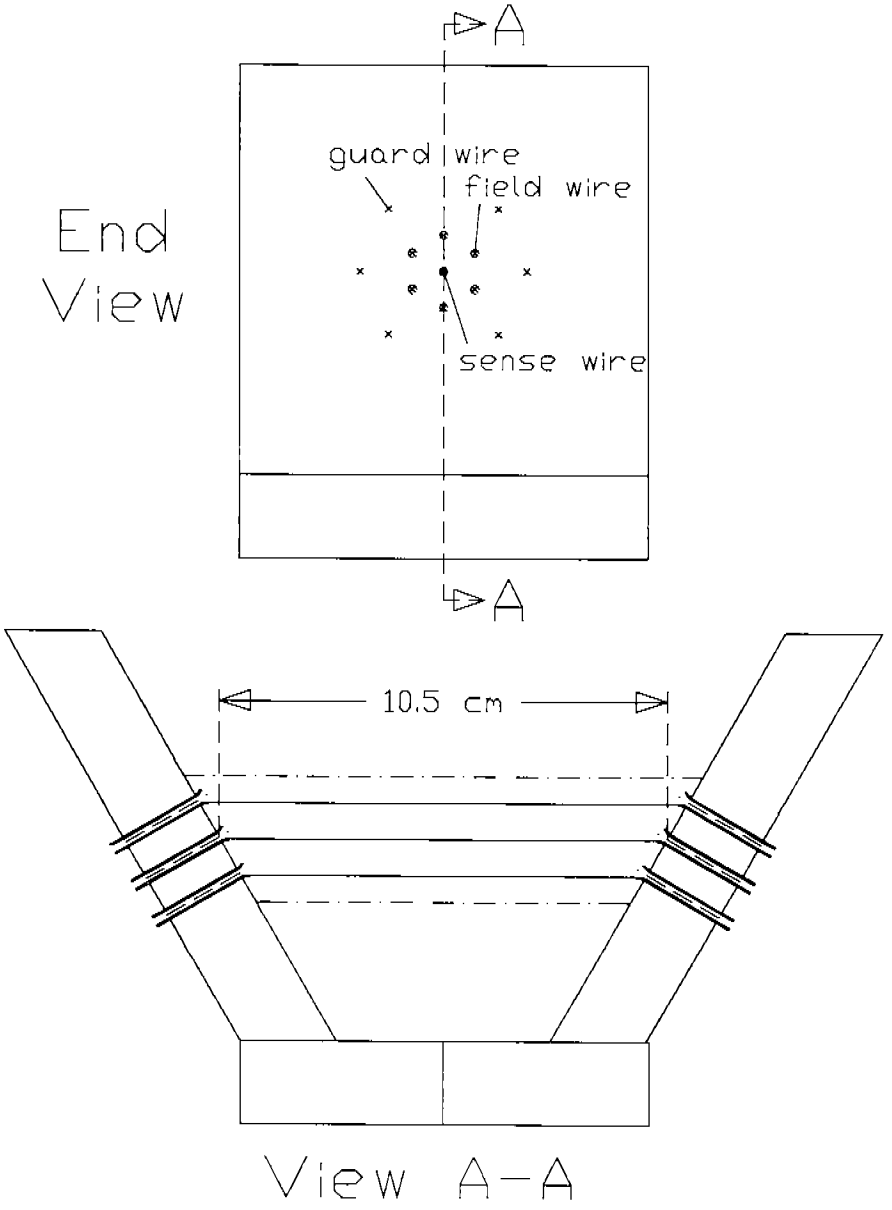

Figure 4.1: Schematic of single-cell prototype constructed with Stesalit 4411W endplates. Top view indicates wire layout as seen for the end. Bottom view shows a cross section through the center of the drift cell with wires and trumpets shown but not crimp pins. Dash-dot lines indicate guard wires.

1 MΩ resistor with a 220 pf capacitor to ground as close to the wires as possible (fig. 4.2). The sense wire was capacitively coupled to the standard CLAS preamp, or SIPP, through a 220 pf capacitor with a 10 kΩ resistor to ground on the SIPP side of the capacitor. The SIPP was powered as shown with 5 V through the standard CLAS voltage regulator. The SIPP signals were processed by sending both negative and positive outputs to a VPI postamp. This unit acts as difference amplifier by subtracting the positive signal from the negative thus removing any post-SIPP noise.

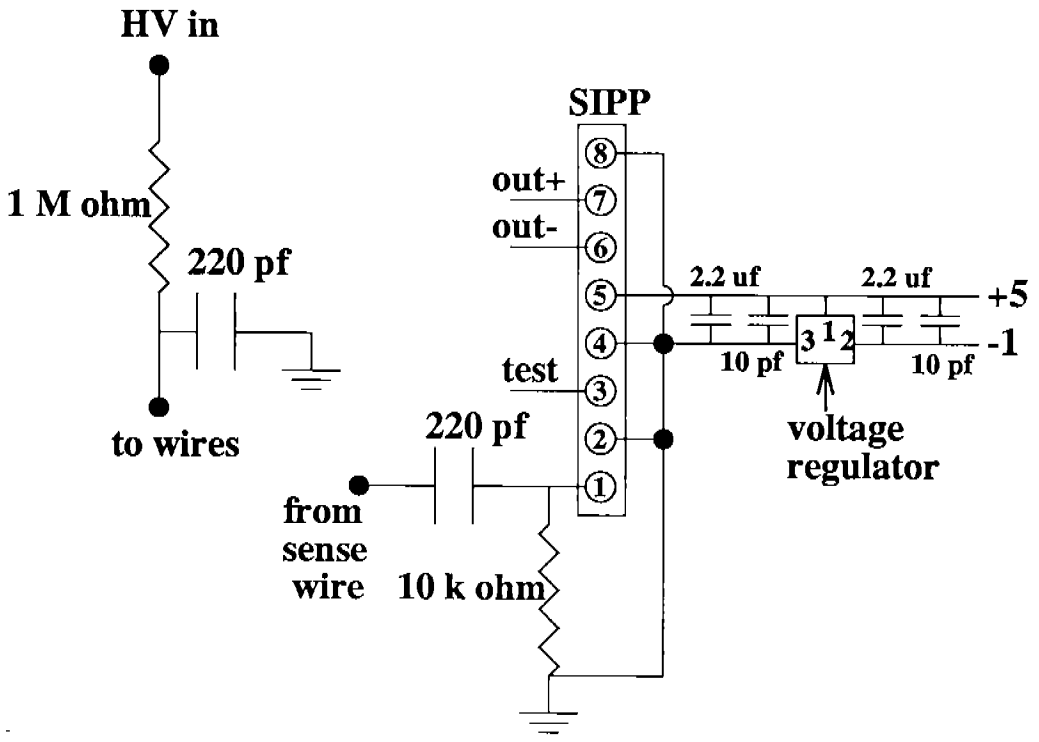

Figure 4.2: Single-cell prototype on-board electronics. Upper left: Typical HV side connections. Right: Sense wire readout side connections with pin numbers of the standard CLAS SIPP and low-voltage regulator indicated.

4.2 Early Observations

The SIPP output connections were constructed such that we could look at either outputs individually before the post-amplification stage. This provided us with the ability to quantify unprocessed signals and diagnose early problems. The nominal operating conditions had a 50/50 Argon/ethane gas mixture (by weight) flowing at a large but undetermined rate through the chamber with voltages of $V_s = +1700$ V, $V_f = -900$ V, and $V_g = +600$ V (sense, field, and guard voltages respectively). The signal from the positive output of the SIPP for a ^{90}Sr beta source was approximately 10-40 mV with a 50 ns rise time and 150 ns fall time.

We also observed an intermittent bipolar fast noise signal of about 40 mV (peak-to-peak) and less than 20 ns in duration. The frequency of this signal increased when warm, damp air was blown across the circuit boards and the exterior of the endplates. In some cases this caused the leakage current of the sense wire to exceed the trip point of the power supply which was set at 800 nA. By cleaning the circuit boards and chamber exterior, coating all of these surfaces with a conformal coating, and rearranging electronics connections to maximize distances between HV points and ground we were able to eliminate these "micro-breakdowns". This points out that great care must be exercised in the design and construction of the final on-board electronics to avoid such problems.

Leakage current

As discussed in part III, we want to minimize the dark current across the surface of the endplates. Once the micro-breakdown problems were solved we could measure the amount of current drawn on the HV power supply by the chamber. In principle the measured current is a combination of dark current across the endplates and the current drawn by the wires themselves. We measured the total leakage current of the chamber as a function of time for various operating conditions. At the nominal operating settings of $V_s = 1750, V_f = -935, \text{and} V_g = 612V$, the sense-wire leakage current remained between 60 and 100 nA over a 140 hour period with a ^{90}Sr source producing a rate of approximately 400 Hz in the chamber. The variation in the current over time was slow (10-20 nA/day) and is likely related to the humidity of the surrounding air. We also found a linear relationship between

the total voltage ($V_t = V_s - V_f$) and the current drawn over the likely operational range of the chamber of $2685 \leq V_t \leq 3065V$.

Characteristics of short drift-distance events

The signal characteristics of short-distance events (events that cross the drift cell near the sense wire) were observed to be significantly different from longer distance events. (The relative terms "short" and "long" are highly dependent on the total voltage between the sense and field wires but short generally refers to distances less than 1/4 of the cell radius.) In such an event, a small fraction of the total ionization is left near the wire resulting in a smaller short-time component to the signal. Ionization from the event that was deposited farther from the sense wire will eventually drift to the wire producing a larger signal at later times. The effect, depicted schematically in fig. 4.3, will be a signal with a similar integrated charge (area under the curve) to a long-distance event but with a much longer rise time. If a simple threshold discriminator were used for timing purposes, the short-distance event would trigger the discriminator at later times (relative to the start of the signal) than long-distance events thus artificially shifting the events to longer drift times.

Of course, the size of the shift depends on the discriminator threshold, the gain of the chamber, and the primary ionization density (energy loss) of the incident particle. If the chamber voltage is set sufficiently high or the threshold sufficiently low, then the effect described here will be minimized. There are potential problems with raising the chamber voltage enough to increase the gain so that ionization left near the sense wire triggers the discriminator. This includes breakdowns within the chamber or on the circuit boards, saturating the SIPP, or overshooting the efficiency plateau. The problem with using a low discriminator threshold is the danger of triggering on electronic noise.

We found that the best solution was to use two levels of discriminator thresholds for the chamber signal. One threshold is set very low so that the slow rise-time component of short-distance events can trigger the discriminator soon after the signal begins, thus minimizing the shift. Since this discriminator level is in the noise, a second threshold is set well above the noise but below the level of all valid signals.

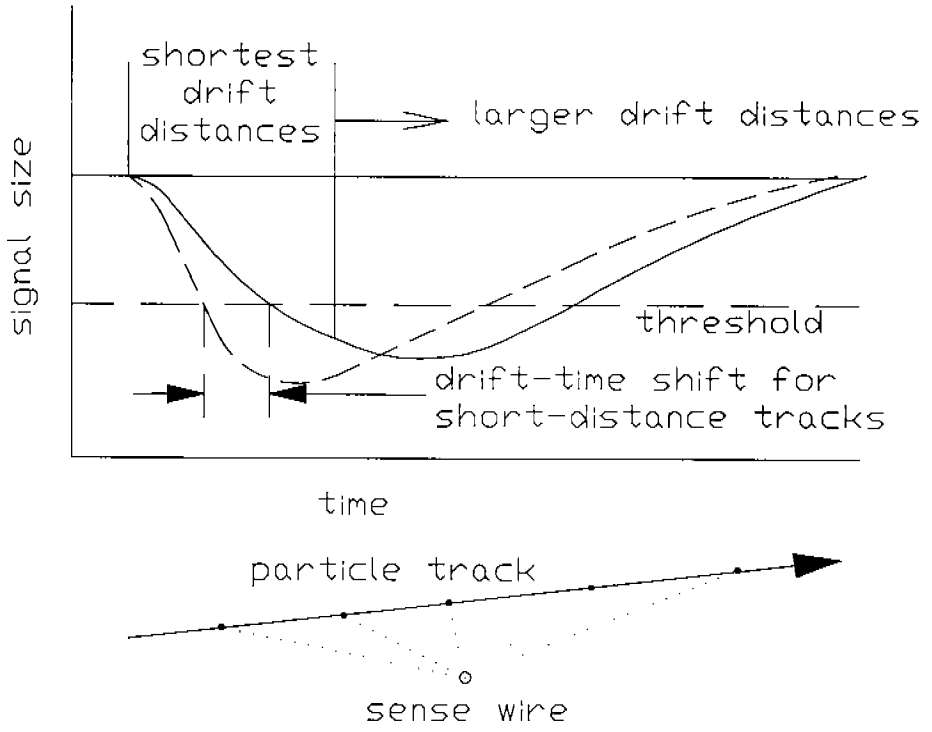

Figure 4.3: Top: Post-amplified sense-wire signals. Solid line is typical of events that occur near the wire. Dashed line for long-distance events. Bottom: Distribution of ionization for short-distance events with drift paths indicated by dotted lines.

A logical AND of these signals – with the low-level trigger defining the timing – will give a trigger which comes at the same time with respect to the arrival of the first drift electrons at the sense wire regardless of where the event occurs in the cell.

4.3 Efficiency Plateau

The prototype was efficiency plateaued using a single 1" wide by 1/4" thick plastic scintillating "finger" which covered the entire length of the sense wire as

a trigger and the ^{90}Sr radioactive source. The source was placed so that the illuminated region of the drift cell was less than half of the cell diameter and approximately centered on the wire both laterally and longitudinally. That is, drift distances greater than about 0.5 cm were excluded as were tracks that traveled near the endplates. The efficiency was calculated to be the ratio of valid chamber triggers divided by the number of scintillator triggers. The resulting plateau curves are shown in figure 4.4. The measured efficiency is very strongly dependent on the high-level discriminator threshold for $V_t < 2850V$ as is demonstrated by the three dramatically different curves displayed in the figure. This is simply due to the fact that there is less gain at lower biases and the smaller energy loss signals don't trigger the discriminator.

Because we used a single scintillator rather than a coincidence of two (or more) scintillators, our trigger contained some noise. This noise reduced the maximum efficiency we could measure from the wire chamber. (ie: If 8% of the scintillator triggers were noise, then our maximum measurable efficiency would be 92%.) The wire chamber efficiency depended strongly on the scintillator threshold. Nonetheless, the method gives a reproducible relative efficiency of 92% above 2850 V and also indicates that, with an appropriate wire chamber discriminator threshold, full efficiency can be achieved at total biases above 2700 V.

This method also does not allow the measurement of the position dependence of the efficiency because of the large area illuminated by the source and seen by the scintillator. To overcome the problem of poor spatial definition of the triggering particles we constructed a hodoscope of scintillating fibers to be used as a trigger. The hodoscope consisted of 2x2 mm^2 scintillating plastic fibers approximately 10 cm long which were arranged into two bundles of five fibers each. The hodoscope was placed on one side of the chamber with the fibers running parallel to the edge of the endplate as shown in figure 4.5. With the hodoscope on one side of the chamber and the ^{90}Sr source on the other, we can define tracks through the chamber with about 1 mm resolution in the horizontal plane of the sense wire and parallel to the endplate. However, the resolution is dominated by the electron multiple scattering of 3 mm FWHM. The finger scintillator was placed above the hodoscope with the long axis centered on the sense wire. A coincidence between

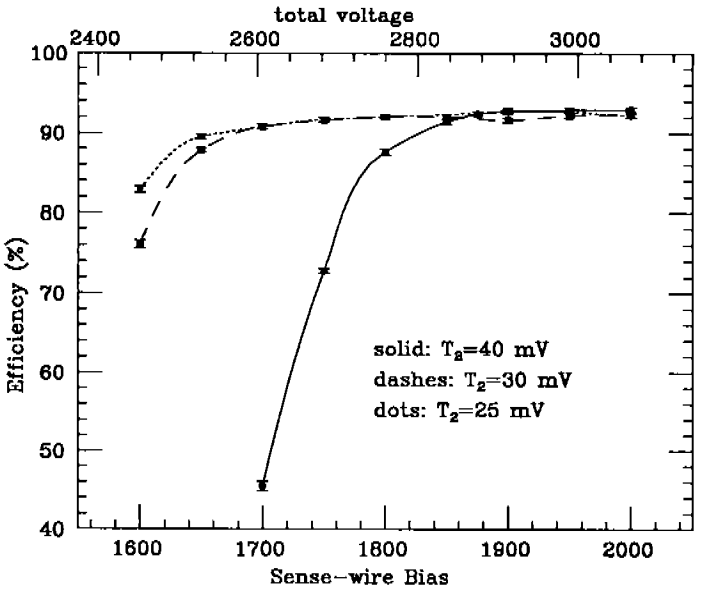

Figure 4.4: Chamber efficiency as a function of chamber bias for three settings of the high-level sense-wire discriminator threshold T_2. Curves are included to guide the eye.

the hodoscope and the finger provided a relatively noise-free trigger.

The efficiency as a function of distance from the endplate is shown in figure 4.6. We see that the chamber is nearly dead at 5 mm from the endplate and does not becomes fully efficient until 14 mm from the endplate (although this might be slightly reduced if the 3 mm FWHM resolution is unfolded from the data). The "full" efficiency discovered here was only about 84% – substantially below the 92% seen earlier – however the efficiency is clearly saturated beyond 14 mm. The low efficiency is probably due to the increased noise levels of the hodoscope relative to the finger scintillator used in the earlier tests.

4.4 Position Dependence of Gain

The previous tests indicated that the low efficiency region of the drift chamber extended somewhat beyond what we had hoped. Our design goal for the region

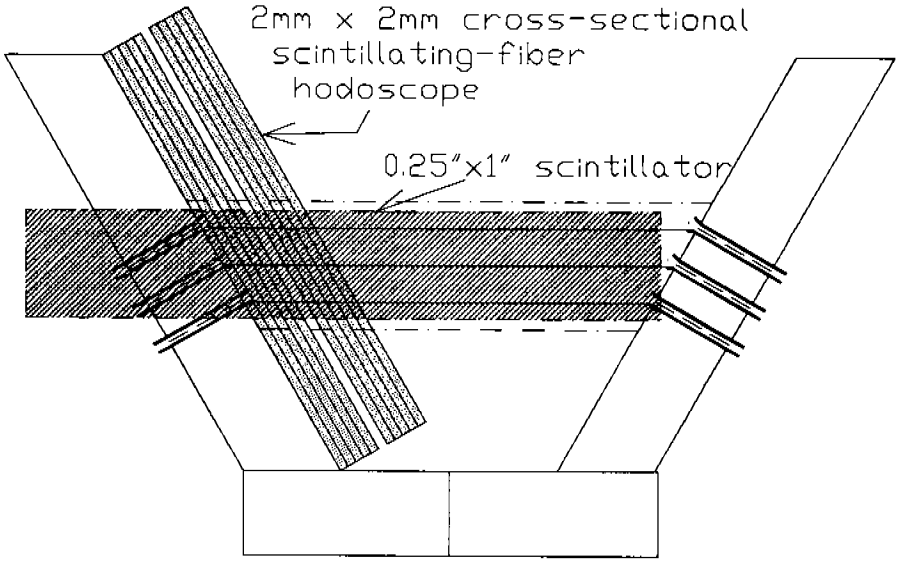

Figure 4.5: Top view schematic of test setup to measure efficiency near the endplate. Both scintillators are on the near side of the chamber and the source (not shown) is on the far side.

2 drift chambers was to have full efficiency at about 10 mm from the endplate. This is about what one would expect if we assume that the chamber were fully efficient just beyond the tip of the shortest field wire's trumpet. We would naively expect that the shape of the electric field is nearly distortion free at that point thus yielding characteristics similar to those near the center of the chamber.

In an attempt to recover some of the less efficient volume of the chamber a field-shaping grid of 120μ wire was placed on one endplate as shown in figure 4.7. The intent was to shape the electric-field lines near the endplate so that the field in this region is similar to the field near the central portion of the chamber. The grid was grounded for this test and variations in the relative voltage between the sense wire and the grid was adjusted by simply changing the sense-wire bias with corresponding changes in the field and guard wires. The other endplate was left alone.

The tests described in section 4.3 do not provide any information about the chamber's response as a function of distance from the sense wire. At a specified

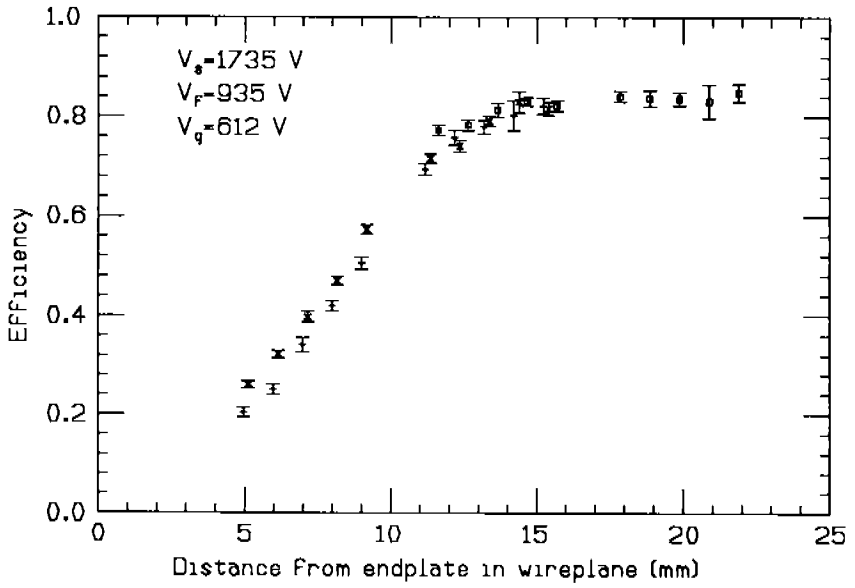

Figure 4.6: Chamber efficiency as a function of distance from the endplate for chamber bias as indicated.

distance from the endplate one should expect different responses for different distances from the sense wire. An attempt to use the two bundles of the hodoscope with their long axes orthogonally oriented to provide finer track definition was unsuccessful.

We used the CEBAF Detectormeisters' collimated x-ray source to map the wire chamber's response near the endplates. A schematic of the x-ray test setup is shown in figure 4.8. The x-ray tube was mounted on a two-axis translation system with the x-axis defined to be parallel to the sense wire and the y-axis perpendicular to the sense wire. The x-ray tube provides a continuous current of x-rays with a beam spot at the sense wire of approximately 1 mm diameter. The system allowed us to illuminate specific regions of the chamber with a well defined beam.

The only measurement available to us to characterize the chamber's response was the measurement of the current drawn by the sense-wire HV power supply. Attempts to look at signals failed miserably due to the enormous noise induced by the x-ray generator. In principle, the current drawn is roughly proportional to both chamber gain and efficiency. Of course gain and efficiency are also correlated

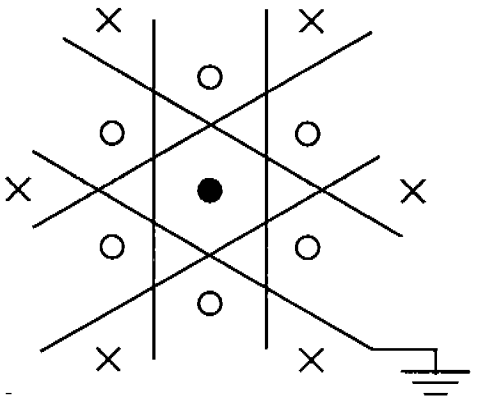

Figure 4.7: Layout of prototype electrodes. Relative orientation on the endplate of the sense wire (filled circle), field wire (unfilled circles), guard wire (crosses), and shaping grid are shown.

so the true functional relationship between gain, efficiency, and current draw is complicated.

Detailed scans in both x and y dimensions were done for a large range of relative grid voltages. For brevity, figure 4.9 shows the results of scans in the x dimension (parallel to the wire) for y = $\pm$2.5 mm (positive is above the wire when looking at figure 4.8). As a reference, a scan was done near the endplate without the grid (labeled as right end) for nominal settings of the voltages. At all sense-wire voltage settings the voltage difference between sense and field wires was maintained at 2683 V. A slight variation in the overall gain in the central region of the chamber was seen at the different voltage settings so the currents have been scaled so that all curves agree at large distances from the endplates. The distance from the endplate is measured parallel to the wire.

We compared the current drawn near the gridded endplate with the current drawn near the ungridded endplate to crudely compare the chamber efficiency near the endplates. If the chamber was much more efficient near the gridded endplate than the ungridded endplate, we would expect to see a significantly higher current drawn near the gridded endplate. Conversely, if the current drawn is similar near the two endplates, then the efficiencies should be similar. We investigated the

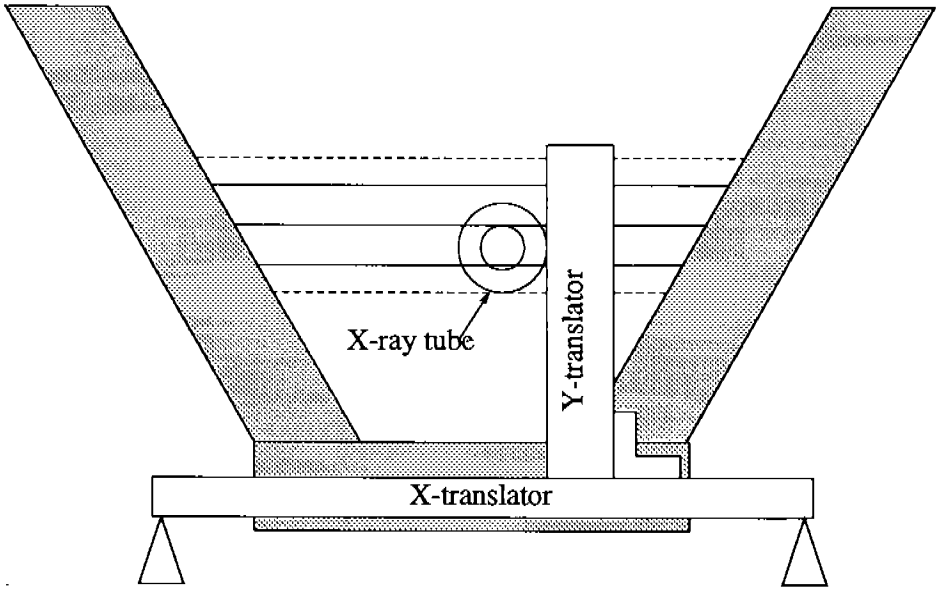

Figure 4.8: Schematic of the prototype chamber/x-ray source test setup. The x-ray beam points into the paper in the figure and can be moved by stepping motor control of the x- and y-translators.

effects of different grid voltages by biasing the sense, field and ground wire voltages (eg: raising the sense, field and guard wire voltages 100 V is equivalent to leaving them unchanged and putting the grid at -100 V).

We see that for all but the highest bias voltage setting the current draw near the gridded endplate (left end) was lower than for the non-gridded end. At the highest setting the current draw was slightly higher than for the non-gridded end suggesting that the response near the endplate improved slightly. The increase in the current draw was small – effectively moving the response curve toward the endplate by less than a millimeter. However, when the x-ray source was within 8-10 mm from the endplate the current rapidly grew beyond the limit of the supply suggesting a runaway gain (at least for the ionization flux used in this test). In short, any improvement of the chamber characteristics near the endplate by adding a shaping grid is not worth the excessive effort and expense that would be incurred during the construction of the region 2 chambers.

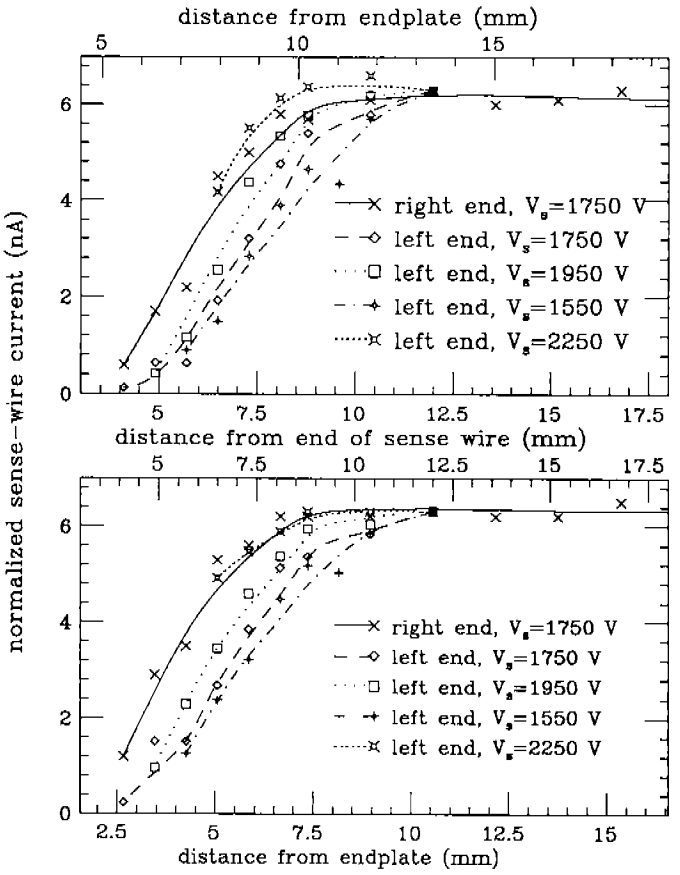

Figure 4.9: Current drawn on the sense-wire power supply versus distance from the endplate (parallel to the wires) for sense-wire voltage settings as labeled. Top figure is for the scan above the wire and bottom figure is for the scan below the wire. The systematic uncertainty in the current measurement is about 0.1 nA.

Bibliography

[1] 2020 Rigid Materials (corporate flyer), Stesalit AG, CH-4234 Zullwil SO.

[2] Gretchen Doolittle, CEBAF technical drawing numbers 66210-E-01150 and 66210-E-01149.

[3] Walter Tuzel, CEBAF finite element analysis calculations.

[4] "Conceptual Design Report – Basic Experimental Equipment," CEBAF April, 1990.